

Metamorphosis of the ZnO buffer layer thicknesses on the performance of inverted organic solar cells

M. Z. Sahdan¹ · M. F. Malek^{2,3} · M. S. Alias¹ · S. A. Kamaruddin¹ · C. A. Norhidayah¹ · N. Sarip¹ · N. Nafarizal¹ · M. Rusop^{2,3}

Received: 27 February 2016 / Accepted: 23 July 2016 / Published online: 29 July 2016
© Springer Science+Business Media New York 2016

Abstract This study investigates the zinc oxide (ZnO) buffer layer thickness in the photovoltaic performance of inverted organic solar cells (OSCs) based on an active layer blend of poly(3-hexylthiophene), (P3HT) and [6, 6]-phenyl-C61 butyric acid methyl ester, (PCBM). The ZnO buffer layer acts as a protective layer to prevent the photoactive layer interface by UV light from oxidation. Besides, it reduces the energy barrier to easily transfer electrons between the collecting electrode and the organic acceptor lowest unoccupied molecular orbital level. The buffer layer block holes in P3HT from recombining with electrons in the collecting electrode. The X-ray diffraction analysis show that the constant orientation of the grains according to the *c*-axis perpendicular to the substrate surface. The optical measurements indicated that all samples have a transmission higher than 60 % in the visible range. A slight shift of the absorption edge toward the small wavelengths was observed as the thickness increased to over 250 nm. The electrical measurements depended on thickness. The resistivity decreased from 5.45 to $4.98 \times 10^{-3} \Omega \cdot \text{cm}$, and the mobility increased from 1.66 to $1.71 \times 10^{-1} \text{ cm}^2/\text{Vs}$ when the thickness increased from 65.6 nm to 107.0 nm. This behavior was explained by the

crystallinity pattern. The optimization of the ZnO buffer layer caused the short circuit current density to vary from 0.287 to 1.599 mA/cm² and the fill factor to range between 19.08 and 24.55 %. This result increased the power conversion efficiency from 0.007 to 0.043 %. The photovoltaic performance of inverted structure OSCs is strongly dependent on the ZnO buffer layer thickness.

1 Introduction

Organic solar cells (OSCs) have attracted tremendous attention among researchers considering the increasing energy requirements. OSCs have drawn immense interest and have become a promising energy technology to overcome the rising global energy demand challenge. This new technology represents low-cost generation, easy processability, and scalable alternative to high-cost conventional silicon-based solar cells. Compared with traditional inorganic solar cells, OSCs suffer from limited environmental stability. This inherent weakness bars the commercialization process.

In conventional OSCs devices, *p*- and *n*-type materials are mixed, forming a nanoscale interpenetrating network to enhance charge separation by providing a large interfacial area, resulting in a photocurrent increment [1]. This structure is fabricated using a transparent conductive anode (TCO), an active layer, and a low work function metal cathode. However, the *p*- and *n*-type materials have to be in contact with the cathode and anode leading to a recombination at the electrodes [2]. This has been overcome by inserting a hole blocking layers at the cathode such as the TiO₂ [3] or ZnO [1, 4] because of their low hole conductivity and high electron mobility. An electron-blocking layer such as PEDOT:PSS at the anode has been deposited

✉ M. F. Malek
firz_solarzelle@yahoo.com

¹ Microelectronics and Nanotechnology - Shamsuddin Research Centre (MiNT-SRC), Universiti Tun Hussein Onn Malaysia (UTHM), 86400 Batu Pahat, Johor, Malaysia

² NANO-ElecTronic Centre (NET), Faculty of Electrical Engineering, Universiti Teknologi MARA (UiTM), 40450 Shah Alam, Selangor, Malaysia

³ NANO-SciTech Centre (NST), Institute of Science (IOS), Universiti Teknologi MARA (UiTM), 40450 Shah Alam, Selangor, Malaysia

on top of the TCO. Unfortunately, this layer is prone to degradation as it absorbs moisture related to poor environmental stability [5, 6]. Furthermore, the hygroscopic PEDOT:PSS layer may etch the TCO layer given the acidity of the PSS [6]. In addition, aluminum (Al) was normally used as back electrode in this type of solar cells; however, these devices show instability in non-encapsulated devices because of the rapid oxidation of the low work function electrode [7, 8].

The “inverted” structure geometry of the device, wherein the charge separation and collection are reversed in contrast to the conventional structure, is proposed to solve this instability. By reversing the charge collection, this configuration eases fabrication because an air-stable and high work function Au electrode replaces the air sensitive Al electrode in collecting holes from the active layer [9]. Furthermore, the PEDOT:PSS is replaced by a metal oxide to enhance structure stability. ZnO is the most suitable material as cathodic and hole-blocking layers owing to its high electron mobility, good optical transparency to visible light, compactness, good blend-wettability, and improved environmental stability [10–12].

Several extensive researches have lately focused on OSC performance. Noh et al. [13] has fabricated an inverted polymer solar cell using ZnO as an electron transport layers prepared by spray pyrolysis. They obtained a solar cell with a 3.22 % efficiency using ZnO annealed at 350 °C. Moreover, inverted polymer bulk heterojunction (BHJ) solar cells with a 5.29 % power conversion efficiency has been fabricated using *n*-type mixed (ZnO:Cs₂CO₃) electron transport layer and blend of poly (3-hexylthiophene):Indene-C60 bisadduct [14]. The good performance of their device is attributed to the improved interfacial contact between the photoactive and electron extraction layers, the low leakage current, and the suitable surface morphology for electron extraction and transport.

Yu et al. [15] applied a polyvinylpyrrolidone (PVP) thin film on top of Al-doped ZnO as an interface modifier in inverted polymer solar cells. Utilizing PVP reveals a significant increase in solar cell conversion efficiency between 2.86 and 4.08 %. Furthermore, Thambidurai et al. [16] reported the effect of In doping on OSC performance. They found that the solar cell with 6.74 % In-doped ZnO exhibited a power conversion efficiency of 5.58 %. The morphologies and thicknesses of metal oxide layers in inverted BHJ solar cells significantly influence the performances of OSCs [17, 18]. In this study, inverted-type OSCs are fabricated using different ZnO thicknesses to investigate the performances and energy efficiencies. Examining the effects of thickness, structural morphology, optical and electrical properties of the buffer layer is crucial for a maximum carrier transport.

2 Experimental details

2.1 ZnO buffer layer growth deposition

In this experiment, indium tin oxide (ITO) substrates with a dimension of 20 mm × 20 mm × 1 mm were cleaned ultrasonically in acetone for 3 min. These substrates were further cleaned with deionized water to remove the residual contaminant. The substrates were subsequently dried by a stream of nitrogen gas. The ZnO precursor for the sol–gel preparation was formed by dissolving zinc acetate dihydrate (Zn(CH₃COO)₂·2H₂O) and monoethanolamine (MEA, C₂H₇NO), mixed with exactly the same mole ratio, in 2-methoxyethanol (C₃H₈O₂). The details of the sol preparation and the deposition process have been revealed in a previous report [19]. The chelating agent MEA increases solution stability through the formation of soluble acetate and MEA complexes. The zinc acetate concentration was fixed at 0.4 mol/L. The ZnO precursor solution was stirred and aged for a certain time prior to deposition. After being aged, the ZnO precursor was spin coated on the ITO substrate by spin-coating technique at room temperature with a speed of 3000 rpm for 30 s. After spin coating, the samples were heated in a furnace to evaporate the solvent and to remove the residual organic material. Each sample was subjected to this procedure between 1 and 10 times to obtain various buffer layer thicknesses. After coating the required number of layers, the ZnO thin film was annealed at 500 °C for 1 h before air cooling at room temperature. The structural morphologies and thicknesses of the films were characterized using a field emission scanning electron microscope (FESEM, model: JEOL JSM 6701F) with an operating voltage between 0.5 and 30 kV and a transmission electron microscope (TEM, model: FEI's TecnaiTM G2). The additional supporting thickness measurement was estimated by KLA Tencor P-6 profilometer. The thin film crystal structure properties and phases of ZnO buffer layers were investigated using a PANalytical X'Pert³ Powder X-ray diffractometer in a standard θ – 2θ Bragg–Brentano geometry configuration with a monochromatic Cu K α ($\lambda = 0.154$ nm) radiation. Scan pattern data were collected between 25° and 60° with 0.02° step lengths. The optical transmittance properties of the sample were characterized using a UV–Vis–NIR spectrometer (model: Varian Cary 5000), whereas the film thicknesses were verified from the cross-sectional of the samples by FESEM characterization. Hall mobility, carrier concentration, and electrical resistivity were evaluated using ECOPIA HMS-3000 Hall measurement system.

2.2 Fabrication of solar cell devices

The ZnO buffer layer growth on the ITO substrate was then initiated for the device fabrication. The active later solution was formed by dissolving regioregular poly(3-hexylthiophene) (P3HT) and [6,6]-phenyl-C₆₁ butyric acid methyl ester (PCBM) in a vial of 1,2-dichlorobenzene (C₆H₄Cl₂), mixed with a weight ratio of 1:1. The P3HT and PCBM purchased from Sigma Aldrich were used as is with no further purification. The solution in the vial was stirred overnight at room temperature under the dark. The P3HT:PCBM blend was then spin-coated on the ZnO buffer layer films and preheated at 60 °C for 5 min. The device structure was completed by depositing a gold (Au) layer as the counter electrode. Au anode was thermally evaporated through shadow mask to control the work function between the P3HT HOMO level and the metal electrode energy level. Finally, the photovoltaic device was thermally annealed at 150 °C for 5 min. The ITO/ZnO buffer layer/P3HT:PCBM/Au inverted OSCs layout is illustrated in Fig. 1. The current density versus voltage (J–V) was measured by a Keithley 2420 digital source meter. The photocurrent was generated under air mass 1.5 global (AM 1.5 G) condition with an illumination intensity of 100 mW/cm² from an Oriel Sol 1A solar simulator calibrated with a standard crystalline silicon solar cell.

3 Results and discussion

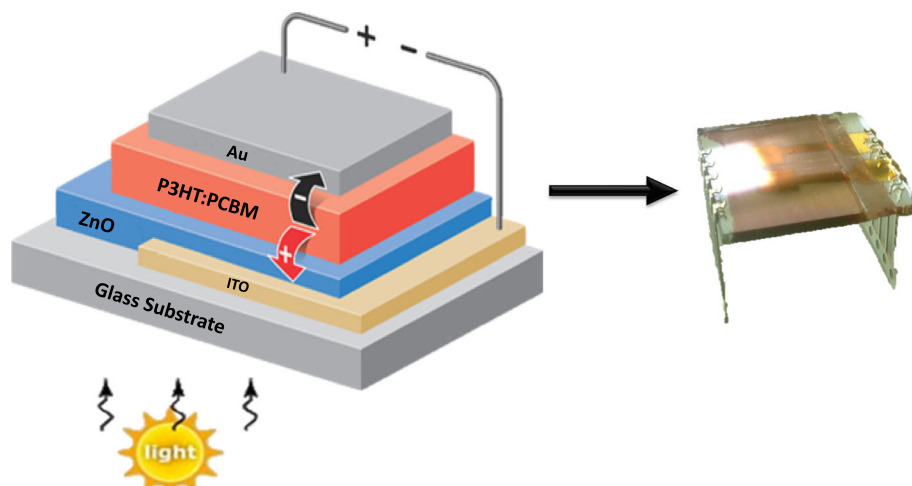
3.1 Properties of ZnO buffer layer

The ZnO buffer layer surface morphology was presented in Fig. 2a–d (100 k magnification at 5 kV applied voltage). The number of buffer layer evidently modifies the surface morphology as the layer changes from 1 to 10 layers. An

abrupt change in the surface morphology of the films can be seen from the FESEM micrographs when the buffer layer increased. The surface of the single ZnO buffer layer is covered with an irregular spherical grain and a porous disorder granular. A more uniform coverage of a faceted granular grain structure with irregular shape appeared as the prevailing porous structure remained evident as the buffer layer increased to three layers. Furthermore, the buffer films observed were deposited with 10 layers, as well as a compact and less porous surface covered by wavy grains. Thus, the number of ZnO buffer layer increases as the voids around the grains decrease and cause a more efficient physical contact. A cross-section image of the ZnO thin film was shown in the inset of Fig. 2 (50 k magnification; 7 kV applied voltage). Owing to an increased in number of buffer layer deposition, the ZnO buffer layer film thickens. The cross-section micrograph reveals the ZnO buffer layer thickness between 65.6 and 521 nm. The thickness variation measured by both FESEM and surface profiler are presented in Table 1. Furthermore, Fig. 2e shows a TEM image of the sample deposited with 10 layers, taken with the film perpendicular to the incident beam. Figure 2f shows a cross section TEM image from a 10-layered ZnO buffer layer and the EDX spectrum recorded in a point of the selected zone. The marked area was divided into several zones and an EDX spectrum was acquired in each zone. The qualitative and quantitative X-ray microanalyses, as well as the maps of the elements were obtained using the recorded EDX spectra.

Figure 3 shows the XRD patterns of the ZnO buffer layer deposited at various thicknesses. All samples exhibited diffraction peaks, which can be indexed as a hexagonal phase ZnO with a wurtzite structure (JCPDS No. 00-036-1451). The ZnO buffer layer structure adhesion to the glass substrate was examined through an ordinary tape peel test using 3 M Scotch TapeTM. None of the films deposited on

Fig. 1 Schematic configuration of the inverted organic solar cell



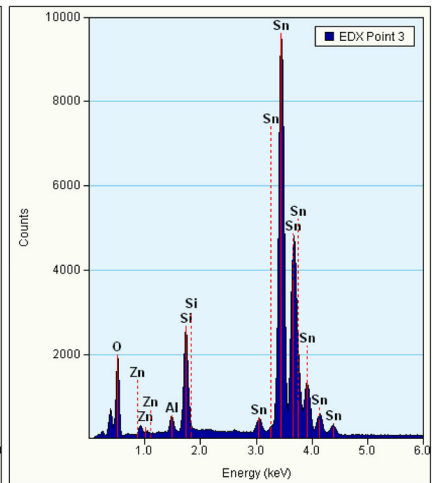
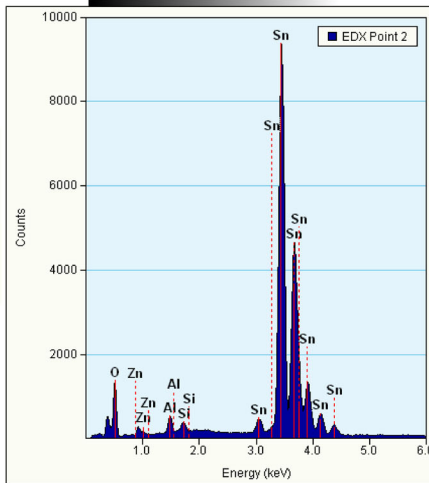
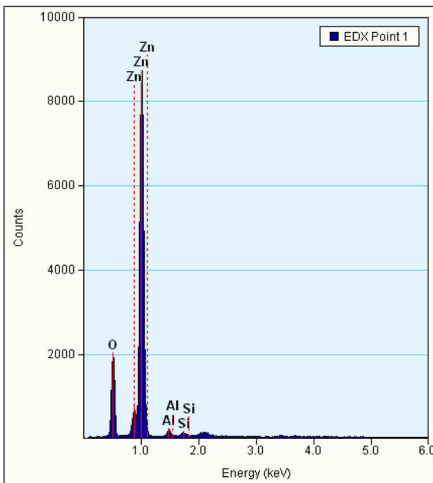
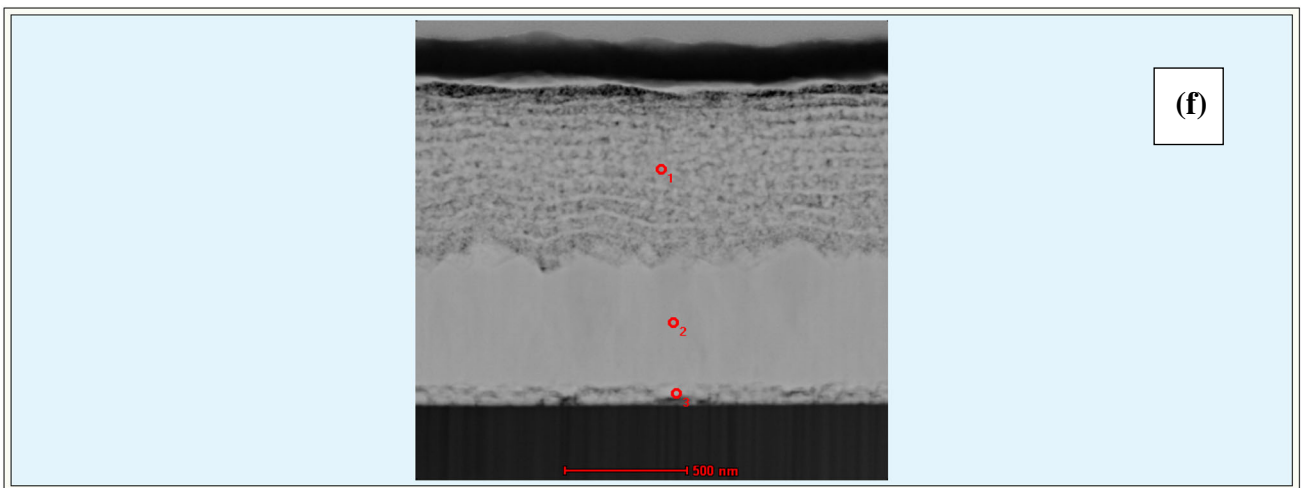
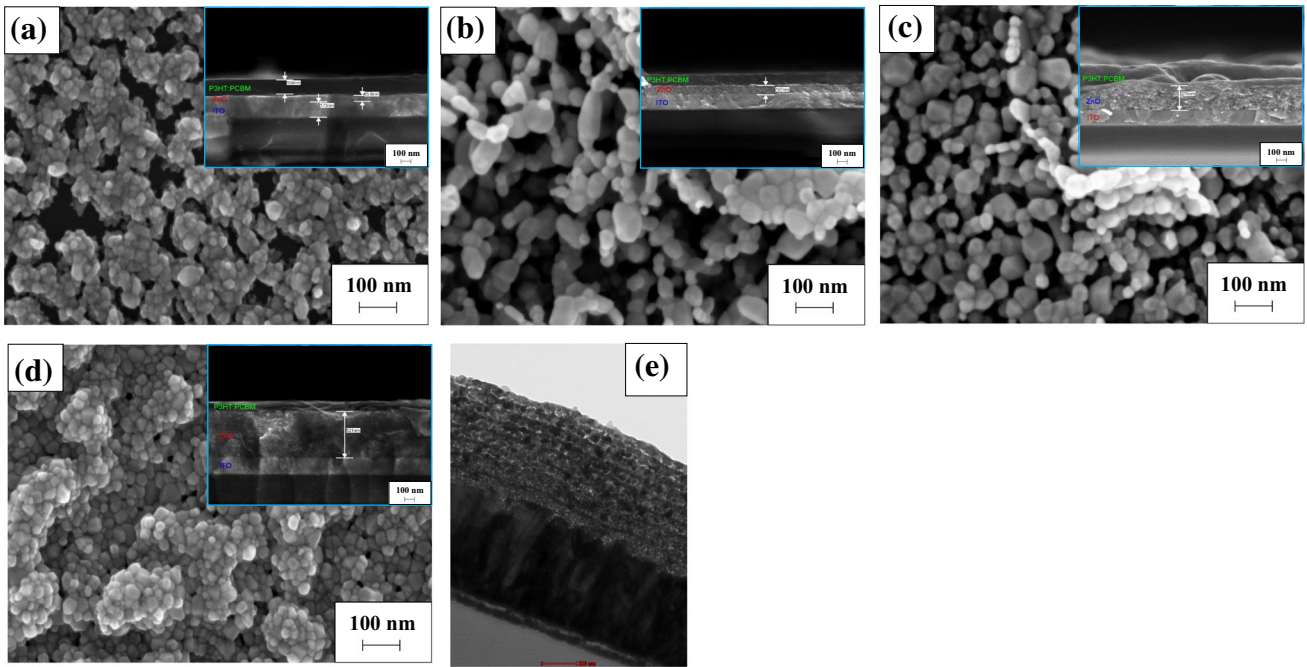


Fig. 2 FESEM morphology (100 k magnification; 5 kV applied voltage) and thickness (50 k magnification; 7 kV applied voltage) of the ZnO buffer layer at various thicknesses **a** 1 layer; 65.6 nm, **b** 2 layers; 107 nm, **c** 3 layers; 276 nm, and **d** 10 layers; 521 nm, **e** TEM image of cross section ZnO buffer layer sample with 10 layers and **f** EDX spectrum recorded in the marked point from the image

glass substrates were removed, which indicated the strong adherence of the films to the glass substrates. The XRD pattern indicates that the five peaks mostly appeared at $2\theta \sim 31.7^\circ, 34.4^\circ, 36.2^\circ, 47.5^\circ,$ and 56.6° corresponding to the (100), (002), (101), (102), and (110) crystallographic planes of ZnO, respectively. All XRD patterns exhibited the strongest (002) orientation peak centered at 34.4° , yielding the highest intensity compared with other peaks. These results verified that these ZnO buffer layers possessed the highly preferred orientation along the *c*-axis or perpendicular to the substrate. The highest intensity of the (002) peak for the ZnO buffer layer was observed deposited at the second layer. As the thickness increased, the (002) peak weakened with the increases in other peaks, which may be attributed to the imperfect ZnO orientation alignment on the substrate. These results indicated the possibility of producing a highly preferred orientation ZnO buffer layer at lower thicknesses. The relative peak intensity orientation $P_{(hkl)}$ of a particular plane (*hkl*) of the ZnO

buffer layer was estimated from its XRD pattern using the following formula (1) [20]:

$$P_{(hkl)} = \frac{I_{(hkl)}}{\sum I_{(hkl)}} \tag{1}$$

where $I_{(hkl)}$ is the (*hkl*) peak intensity, and $\sum I_{(hkl)}$ is the sum of the intensities of all the diffraction peaks of the ZnO buffer layer. The relative peak intensity of the ZnO buffer layer (002) plane is presented in Table 2. A significant increase in the intensity ratio of the (002) peak, $I_{(002)}/\sum I_{(hkl)}$, demonstrated a preferential growth of the material along the *c*-axis crystallographic plane, which introduced the minimum surface energy. The highest relative peak intensity for sample deposited for two layers was 0.713. As the thickness increased to 10 layers, the relative peak intensity significantly decreased to 0.405 probably because of the imperfect crystal orientation and crystal structure observed from the previous FESEM results. The XRD peak intensity of the (002) plane of the ZnO buffer layer relative to the sample grown to 10 layer increases in the sample order, $4^\# < 1^\# < 3^\# < 2^\#$, suggested that a higher degree of preferred *c*-axis oriented was optimum for the sample deposited with 2 layers. The average crystallite size, *D* of the ZnO buffer layer deposited at various thicknesses was obtained by the following Scherrer's Eq. (2) [21–23]:

$$D_{(002)} = \frac{0.94\lambda}{\beta_{(002)}\cos\theta} \tag{2}$$

Table 1 Thicknesses of ZnO buffer layers

Sample	Number of ZnO buffer layer	FESEM thickness (nm)	Surface profiler thickness (nm)
1 [#]	1	65.6	69.3
2 [#]	2	107.0	110.8
3 [#]	3	276.0	283.2
4 [#]	10	521.0	528.7

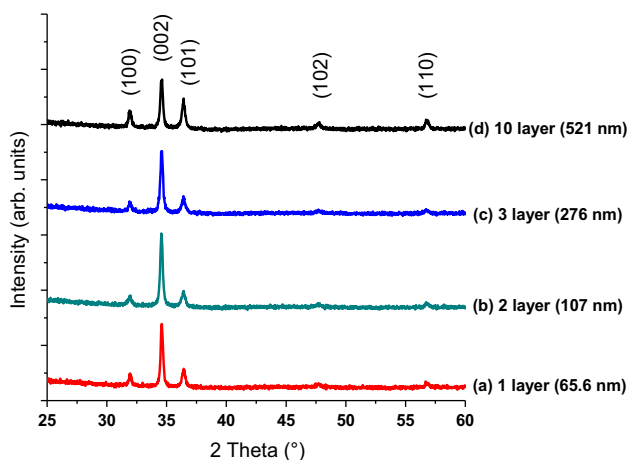


Fig. 3 XRD patterns of the ZnO buffer layer at various thicknesses

where λ , β , and θ are the X-ray wavelength (1.54 Å), the Bragg's diffraction angle in degrees, and the full width at half maximum (FWHM) of the peak corresponding to the " θ " value in the radians, respectively. The FWHM values of the ZnO buffer layer decreased as the buffer layer thickened because of the crystallite size increment. Table 2 summarizes the relative peak intensity to the ZnO (002) plane, the X-ray intensity of the diffraction peak (002) relative to the ZnO buffer layer deposited at the 10th layer, as well as the FWHM and the average crystallite size of the ZnO buffer layer.

The lattice constant, *c* for the ZnO at various layers were calculated according to Bragg's law [24], as follows:

$$2d_{hkl}\sin\theta = n\lambda \tag{3}$$

where d_{hkl} is the spacing between the lattice planes of Miller indices (*h*, *k* and *l*), *n* is the order of diffraction (usually $n = 1$), λ is the X-ray wavelength of CuK_α radiation (1.54 Å), and θ is the Bragg's angle (half of the peak position angle). In the ZnO buffer layer, the following expression relates the lattice plane spacing to the Miller indices and the lattice constant, *c* [25]:

$$\frac{1}{d_{hkl}^2} = \frac{4}{3} \left(\frac{h^2 + hk + k^2}{a^2} \right) + \frac{l^2}{c^2} \tag{4}$$

Table 2 Variation of the structural parameters at various ZnO buffer layers

Sample	Number of ZnO buffer layer	Relative peak intensity (002)	X-ray intensity of diffraction peak (002) relative to ZnO buffer layer deposited at 10th layer	FWHM (degree)	Crystallite size (nm)
1 [#]	1	0.475	1.17	0.4690	18.5
2 [#]	2	0.713	1.76	0.4189	20.7
3 [#]	3	0.642	1.59	0.4141	20.9
4 [#]	10	0.405	1.00	0.3894	22.3

Thus, for a first order approximation, where $n = 1$, the relationship between Eqs. (3) and (4) can be expressed as follows [26]:

$$\sin^2 \theta = \frac{\lambda^2}{4a^2} \left[\frac{4}{3} (h^2 + hk + k^2) + \left(\frac{a}{c} \right)^2 l^2 \right], \quad (5)$$

For the (002) plane orientation, the lattice constant, c_{film} is determined according the following equation

$$c_{film} = \frac{\lambda}{2 \sin \theta} \sqrt{\frac{4}{3} \left(\frac{c}{a} \right)^2 (h^2 + hk + k^2) + l^2}, \quad (6)$$

$$c_{film} = \frac{\lambda}{2 \sin \theta} \quad (7)$$

The lattice constant, c_{bulk} for the strain-free bulk ZnO was 5.2066 Å, as taken from the JCPDS No. 00-036-1451 data card. The lattice parameter values for the ZnO buffer layer were calculated using Eq. (7); they are presented in Table 3. The c_{film} values were observed to be less than the bulk value. Furthermore, the c_{film} was found to increase at the beginning before decreasing and then increasing at higher thicknesses indicating the c -axis compression. The spin-coated strain, ε_{zz} on the glass substrate of the ZnO buffer layer along the c -axis was obtained using the following equation [27, 28]:

$$\varepsilon_{zz} = \frac{c_{film} - c_{bulk}}{c_{bulk}} \times 100\% \quad (8)$$

where c_{film} and c_{bulk} are the lattice constants of the ZnO buffer layer obtained from the XRD data and the standard lattice constant for the unstrained ZnO (JCPDS No. 00-036-1451), respectively. Afterwards, the residual stress on the ZnO buffer layer was calculated to understand the effects of growth time on the preferred c -axis orientation and the crystal-growth properties. For hexagonal crystals,

the residual stress, σ_{film} in the plane of the ZnO buffer layer can be determined by the following biaxial stress model expression [29, 30]:

$$\sigma_{film} = \frac{2C_{13}^2 - C_{33}(C_{11} + C_{12})}{2C_{13}} \cdot \varepsilon_{zz} \quad (9)$$

where ε_{zz} is the average uniform lattice strain along the c -axis and C_{ij} are the elastic stiffness constants of bulk ZnO, i.e., $C_{11} = 208.8$ GPa, $C_{12} = 119.7$ GPa, $C_{13} = 104.2$ GPa, and $C_{33} = 213.8$ GPa [31]. This equation yields the following numerical relationship for stress: $\sigma_{film} = -233\varepsilon_{zz}$ (GPa). The calculated values of strain, ε_{zz} and stress, σ_{film} of the ZnO buffer layer are listed in Table 3. The compressive strain and the tensile stress of the synthesized ZnO buffer layer decreased for the films spun twice with a thickness of 107 nm, which indicated high crystal quality film structure.

The effect of buffer layer thickness on the optical transmittance of the ZnO thin films were studied in the wavelength range of 300–2200 nm. Figure 4 shows that the average transmission in the visible-NIR region ranged from 60 to 99 % depending on the buffer layer thickness. The transmission decreases sharply near the ultraviolet region at about 375 nm because of the band gap absorption. The highest transmittance was obtained for the samples prepared with single layer thickness, whereas the lowest was observed for films deposited at 10 layer thicknesses. The higher transmittance properties of ZnO thin film prepared at less buffer layers may be attributed to the extra voids around the grains discussed in the FESEM results. When the buffer layer number increased (>1 layer), the ZnO thin films were reduced in the optical transmittance because of the optical scattering at the grain boundaries. Moreover, the increased films thickness at higher buffer layers increases

Table 3 Lattice parameters, 2θ position, interplane distance, strain, and stress on the ZnO buffer layer

Sample	Number of ZnO buffer layer	Lattice parameters, c_{film} (Å)	2θ (Degree)	Interplane distance, d (Å)	Strain of c -axis (%)	Stress (GPa)
1 [#]	1	5.1801	34.589	2.5901	-0.506	1.18
2 [#]	2	5.1846	34.559	2.5923	-0.422	0.98
3 [#]	3	5.1837	34.565	2.5918	-0.439	1.02
4 [#]	10	5.1812	34.582	2.5906	-0.487	1.13

the optical scattering which reduces the transmittance of the thin films.

The optical band gap energy, E_g values were estimated from the absorption edges of ZnO thin films as shown in Fig. 5. The absorption edge for the direct interband transition is given by Eqs. (10) and (11), as follows:

$$\alpha hv = B(hv - E_g)^{1/2} \tag{10}$$

$$(\alpha hv)^2 = B\sqrt{hv - E_g} \tag{11}$$

where α is the absorption coefficient, $h\nu$ is the photon energy, E_g is the optical band gap, and B is the energy-independent constant with values between 1×10^5 and $1 \times 10^6 \text{ cm}^{-1} \text{ eV}^{-1}$ [32]. The slight displacement is evident between the absorption edges of the films directly related to the band gap energy variation. The absorption coefficient α should be assumed to satisfy the band gap direct material equation shown in Eqs. (10) and (11) to calculate the band gap energy of the films. The optical energy gap, E_g can then be obtained from the intercept of $(\alpha hv)^2$ versus $h\nu$ for direct transitions. The inset in Fig. 5 shows the band gap variation with respect to the number of buffer layer. Tauc’s plot demonstrated that as the number of buffer layer increased from 1 to 10 layers, the optical band gap energies of the ZnO buffer layer are 3.270, 3.260, 3.275, and 3.280 eV, which closely agreed with the values reported by the other researches on polycrystalline ZnO thin films and the published values of the ZnO electronic transition band gap data [33]. The optical band gap variation at different buffer layer number may be attributed to the optical scattering by grain boundaries and aggregates. Furthermore, the interatomic spacing of ZnO was also reported as being influenced by the strain that affects the band gap energy [34].

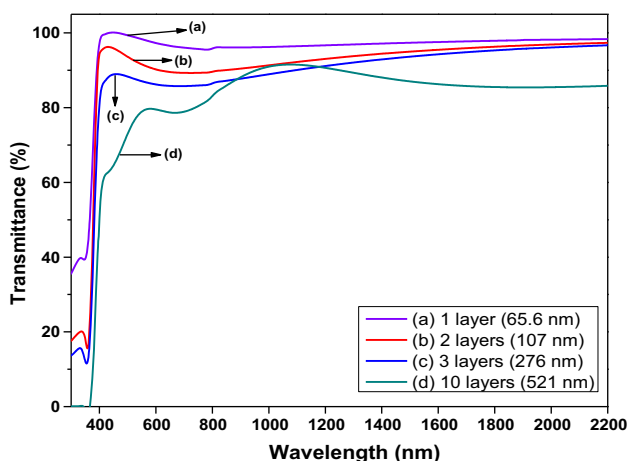


Fig. 4 Optical transmittance spectra of the ZnO buffer layer at various thicknesses

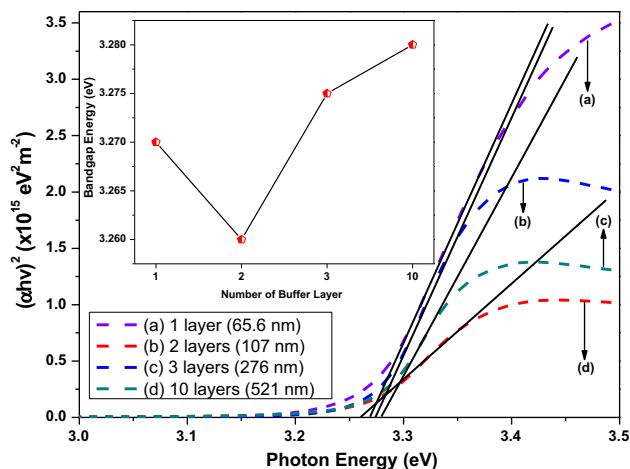


Fig. 5 Optical band gap energy, E_g estimation of the ZnO buffer layer as the function of thickness

The electrical behavior of the ZnO buffer layer relative to their thicknesses was measured through the electrical resistivity and Hall effect (carrier concentration and mobility). The electrical properties were measured with the van der Pauw and Hall method with an applied magnetic field of 0.55 T. The electrical properties of ZnO buffer layer are presented in Fig. 6. The two ranges of thickness included a resistivity that exhibits two different behavior patterns. The first range belongs to the low thicknesses less than $\sim 250 \text{ nm}$ and a decreased resistivity was observed. However, as the thicknesses increased to over $\sim 250 \text{ nm}$, the resistivity starts to increase. The resistivity is closely related to the carrier mobility and concentration through the following relation:

$$\rho = \frac{1}{Ne\mu_H} \tag{12}$$

where N is the carrier concentration, e is the electron charge, and μ_H is the carrier mobility. Table 4 clearly shows that the carrier concentration and mobility depict inverse relations. The results obtained indicate that carrier concentration seems to be less dependent on thickness, whereas resistivity is primarily caused by mobility. The improved crystallinity and the increased grain size were observed from the previous XRD spectra for films with thickness below $\sim 250 \text{ nm}$ that may reduce the carrier diffusion by the grain boundaries, which help increase carrier mobility. However, the crystallinity was reduced as the thicknesses were further increased; at the same time, particle agglomeration was observed in the SEM images. Consequently, these can be the reasons for the decrement in carrier mobility. The relationship showed that the resistivity increased mainly because of the decreased mobility at a thicker buffer layer.

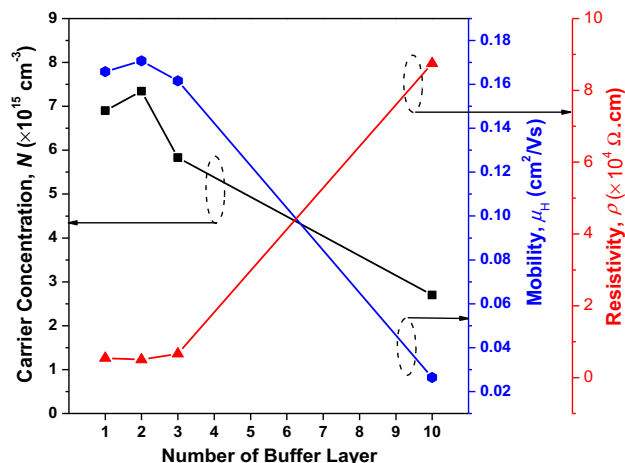


Fig. 6 Thickness dependence of the ZnO buffer layer electrical parameters (resistivity, mobility, and carrier concentration)

3.2 Performance of solar cell devices

Four series of photovoltaic (PV) devices were fabricated in the same method to investigate the influence of the ZnO buffer layer thicknesses on PV performance. The inverted OSCs consisted of a blend polymer donor (P3HT) and a fullerene acceptor (PCBM) deposited in different ZnO buffer layer thicknesses between the ITO as an electron collecting electrode and a metal (Au) as a hole collecting electrode. The ZnO buffer layer acted as a protective layer to prevent direct contact between the ITO and active layers. If the layer is too thin, a penetration between the underlying ITO occurs with the active layer through the buffer layer. Thus, the dependence of the solar cell efficiency on the buffer layer thickness was investigated. Figure 7 shows the current density–voltage (J - V) curves characteristics of the ITO/ZnO/P3HT:PCBM/Au solar cell devices with various ZnO buffer layer thicknesses.

Figures 8 and 9 present the variation of these parameters with the ZnO buffer layer thicknesses. The solar cell power conversion efficiency (PCE or η) and the fill factor (FF) were evaluated with the following relations (13) and (14) [35]:

$$FF = \frac{J_{\max} \times V_{\max}}{J_{sc} \times V_{oc}} \quad (13)$$

$$PCE = \frac{J_{sc} \times V_{oc} \times FF}{P_{in}} \quad (14)$$

Table 4 Electrical resistivity, carrier concentration, and mobility variations with various ZnO buffer layers

Sample	Number of ZnO buffer layer	Resistivity, ρ (Ω .cm)	Carrier concentration, N (cm^{-3})	Mobility, μ_H (cm^2/Vs)
1 [#]	1	5.45×10^3	6.90×10^{15}	1.66×10^{-1}
2 [#]	2	4.98×10^3	7.34×10^{15}	1.71×10^{-1}
3 [#]	3	6.62×10^3	5.83×10^{15}	1.62×10^{-1}
4 [#]	10	8.75×10^4	2.70×10^{15}	2.64×10^{-2}

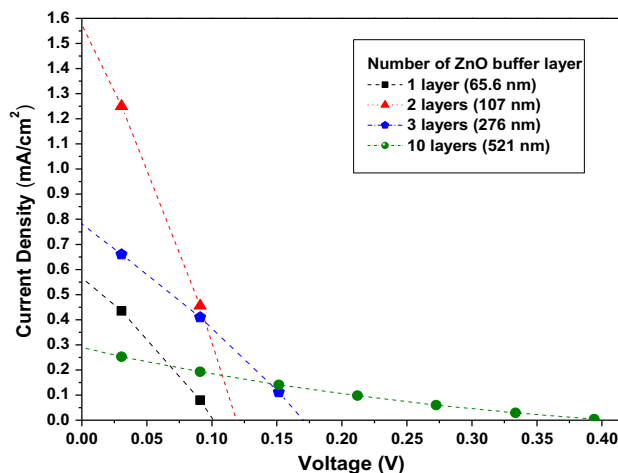


Fig. 7 J - V curves of the inverted organic solar cell based on various ZnO buffer layer thicknesses

where V_{\max} is the maximum voltage, J_{\max} is the maximum current density, J_{sc} is the short circuit current density, V_{oc} is the open circuit voltage, and P_{in} is the incident light power density. The P_{in} was standardized at $100 \text{ mW}/\text{cm}^2$ for a solar cell testing with a spectral intensity distribution matching that of the sun on the earth's surface at an incident angle of 48.2° called the AM 1.5 spectrum [36]. The average performance characteristics of the inverted ITO/ZnO/P3HT:PCBM/Au solar cells are displayed in Table 5. An electron was transferred to the lowest unoccupied molecular orbital (LUMO) by irradiation leaving a hole in the highest occupied molecular orbital (HOMO). Electrons were collected at the transparent cathode and the anode holes.

An increment in V_{oc} was observed in Fig. 8 as the ZnO buffer layer increased. The increased V_{oc} of the devices can be directly correlated with the ZnO buffer layer thickness which introduced more charge carrier in the device. Furthermore, the high V_{oc} clearly indicated that the buffer layer is at a high quality hole-blocking layer. The average PCE value for the ZnO buffer layer with one-cycle spin-coating was 0.007 %. The recombination of the holes in P3HT with the electrons in the collecting electrode can be attributed to the thin ZnO layer. Hence, a direct contact between the ITO and the active layer was possible. Increasing the buffer layer to two improves the J_{sc} value.

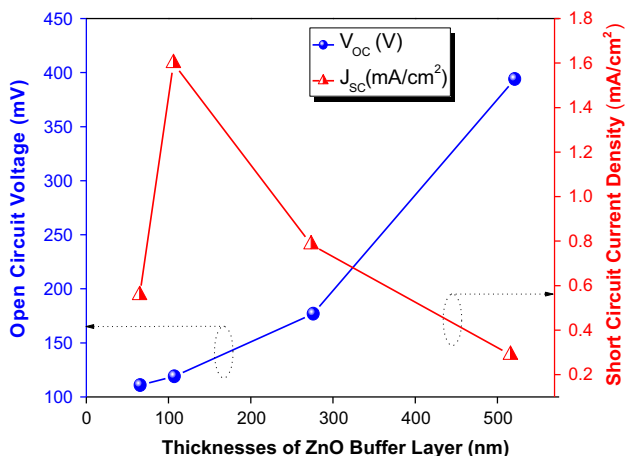


Fig. 8 Short circuit current density (J_{sc}) and open circuit voltage (V_{oc}) variations with different ZnO buffer layer thicknesses in the ITO/ZnO/P3HT:PCBM/Au device configuration

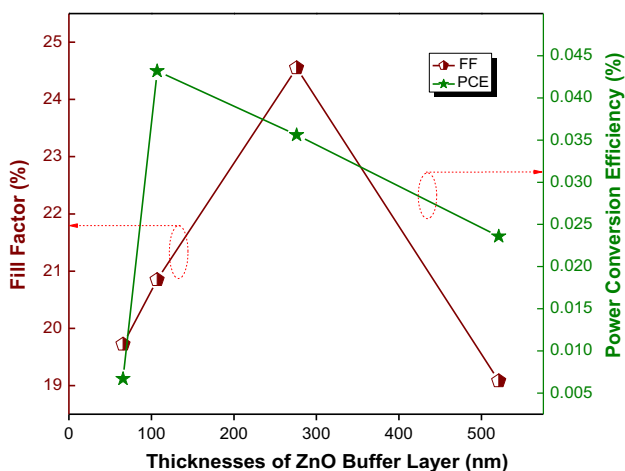


Fig. 9 Power conversion efficiency (η) and fill factor (FF) variations with different of ZnO buffer layer thicknesses in the ITO/ZnO/P3HT:PCBM/Au device configuration

This increase significantly improves the FF of devices, which increases the average PCE to 0.043 %. The ZnO buffer layer completely covered the ITO and provided a better contact to effectively extract electrons from the device. This explains the increased PCE and the dramatic improvement in the device performance. This finding can also be attributed to the band gap energy shift reported above in Fig. 5. However, the spin-coating cycle increased

led to the film thickening, and the power conversion efficiency decreased from 0.043 to 0.024 %. Moreover, a significantly decrease J_{sc} was also observed. In addition, the charge transfers maybe the biggest reason for the increasing J_{sc} , whereas the decrease in J_{sc} at a thicker ZnO buffer layer may be attributed to the poor morphology confirmed in the FESEM images as shown in Fig. 2. In this case, the large amount of zinc ions in the film layers aggregates and prevents charge carriers to transfer through the bulk and to reach the contacts.

Figure 9 shows the variation of FF and PCE values for devices with different ZnO buffer layer thicknesses. An FF increment was observed as the ZnO buffer layer increased from 1 to 3 layers. The PV device composed of the three-cycle spin-coating of the ZnO buffer layer revealed the highest FF at 24.55 %, although the PCE indicated otherwise. This finding is strongly related to the effect of thickness on the charge transport and extraction. Interestingly, the device with the two-cycle spin-coating of ZnO buffer layer showed the highest efficiency at 0.043 % with an FF of 20.85 %, resulting in much improve charged extraction and consequently PCE , even when no significant difference in V_{oc} was observed. However, the FF decreased when we further increased the ZnO buffer layer to 10 layers. The thicker ZnO buffer layer led to a larger contact resistance at the ZnO and active layer interface. Furthermore, the lower FF s of thicker PV devices may be related to the structural defects of the ZnO buffer layer. As a result, the electronic coupling between ZnO and the active layer is declined, which increased the series resistance that impeded electron collection in the OSCs [37, 38]. In addition, the changes in the FF values may also be directly related to the loss in carrier transport (electron) in the interface.

Figure 10 shows the energy band diagram of the inverted OSCs. P3HT possessed a LUMO value of ~ 3.2 eV and a HOMO value of ~ 5.2 eV [39]. In contrast, the PCBM has the LUMO and HOMO values of ~ 3.8 and ~ 6.6 eV, respectively. In the energy band structure, electrons can easily transport to the ITO electrode through the ZnO buffer layer. This diagram shows that the charge separation was carried out in a good manner. When the photon energy struck into the device, an electron was projected from the HOMO to the LUMO, and an electron–hole pair (exciton) was formed moving through the active

Table 5 Device performance of the inverted organic solar cells with varied ZnO buffer layer thicknesses

Sample	Number of ZnO buffer layer	V_{oc} (mV)	J_{sc} (mA/cm ²)	FF (%)	PCE (%)
1 [#]	1	111	0.557	19.72	0.007
2 [#]	2	119	1.599	20.85	0.043
3 [#]	3	177	0.785	24.55	0.036
4 [#]	10	394	0.289	19.08	0.024

layer that creates an electrical current. However, these electron–hole pairs travel a certain distance before it either decays or reaches a boundary with another material. This process is followed by exciton diffusion and dissociation. The ZnO buffer layer conduction band is lower than the LUMO energy levels of the P3HT and the PCBM active layers. An excited electron in the LUMO of the blend polymer transferred to the conduction band of the ZnO buffer layer. The generated electrons were then moved to the ITO contact through a hole blocking layer. In the contrary, the holes were created in the HOMO transfers to the Au electrode. These changes in free energy provided the driving forces for the dissociation of excitons into free charge carriers. Upon dissociation from each other, the electrons migrated by hopping among the LUMO(s) of the active layer toward a low work function electrode, and the holes migrate through the HOMO(s) toward a high work function electrode. Thus, the charge separation was achieved by the asymmetrical work functions of the electrodes. As the ZnO buffer layer was increased with more than two layers, the J_{sc} and PCE decreased. The poor performance of the device with a thicker film indicated the negative role of the excessively increased thickness of the buffer layer. Furthermore, the ZnO buffer layer promoted the formation of continuous uniform PCBM films to prevent the P3HT from contacting the ITO substrates. Thus, this prevents the holes in P3HT from being recombined with the electrons in the collecting electrode [40]. In

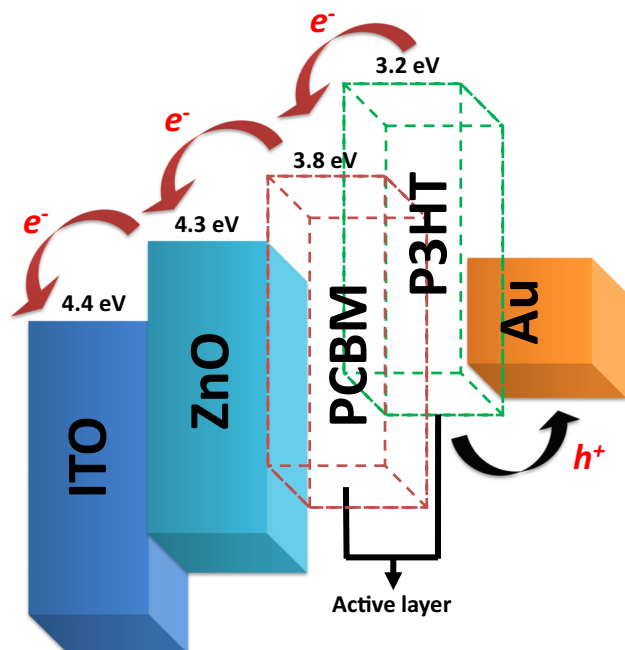


Fig. 10 Energy diagram and charge transfer process of the solar cell device with the ITO/ZnO/P3HT:PCBM/Au configuration

summary, this result enriches our understanding on the buffer layer thickness influencing the inverted OSCs.

4 Conclusion

The performance of ITO/ZnO/P3HT:PCBM/Au solar cells was demonstrated in this work, by varying the ZnO buffer layer thicknesses. The ZnO layer serves as an electron selective and a hole blocking layer in the inverted structure OSCs. The ZnO buffer layer thickness can be controlled by varying the deposition layer number. The ZnO buffer layer should completely cover the underlying ITO surface to prevent shunting. Furthermore, the ZnO buffer layer deposition is necessary in the inverted OSCs to protect the ITO from touching the active layer. This condition is vital to block the holes from recombination with the electrons at the collecting electrode. From the materials properties, the highest relative peak intensity of 0.713 was achieved for sample deposited for two layers. Besides, the details XRD analysis also show that the sample obtained the minimum strain and stress of -0.422% and 0.98 GPa , respectively. The minimum resistivity was achieved at $4.98 \times 10^{-3}\ \Omega\cdot\text{cm}$ with the mobility of $1.71 \times 10^{-1}\ \text{cm}^2/\text{Vs}$ when the thickness at $107.0\ \text{nm}$. In addition, a slight shift of the absorption edge toward higher wavelengths was also observed for that thickness. As a conclusion, the optimum device of the inverted OSC using the ZnO buffer layer that yields power conversion energy of 0.043% with the optimum thickness of $107.0\ \text{nm}$. Numerous developments have to be accomplished in the future to improve the performance of the device through phase processing and fabrication configuration, among others. Thus, this investigation may be applicable to such future production efforts.

Acknowledgments The authors wish to thank the Ministry of Education Malaysia for the financial support through FRGS grant Vote No. 1093 and the Program Ahli Sains dan Penyelidik Muda (PSPM) scholarship under the Universiti Teknologi MARA (UiTM) and the Ministry of Higher Education (MOHE) Malaysia. We also acknowledge Universiti Tun Hussein Onn Malaysia (UTHM) for the technical support.

References

1. B. Gholamkhash, N.M. Kiasari, P. Servati, An efficient inverted organic solar cell with improved ZnO and gold contact layers. *Org. Electron.* **13**, 945–953 (2012)
2. S. Schumann, R. Da Campo, B. Illy, A.C. Cruickshank, M.A. McLachlan, M.P. Ryan, D.J. Riley, D.W. McComb, T.S. Jones, Inverted organic photovoltaic devices with high efficiency and stability based on metal oxide charge extraction layers. *J. Mater. Chem.* **21**, 2381–2386 (2011)

3. J. Weickert, R.B. Dunbar, H.C. Hesse, W. Wiedemann, L. Schmidt-Mende, Nanostructured organic and hybrid solar cells. *Adv. Mater.* **23**, 1810–1828 (2011)
4. N. Espinosa, H.F. Dam, D.M. Tanenbaum, J.W. Andreasen, M. Jørgensen, F.C. Krebs, Roll-to-roll processing of inverted polymer solar cells using hydrated vanadium (V) oxide as a PEDOT:PSS replacement. *Materials* **4**, 169–182 (2011)
5. M. Jørgensen, K. Norrman, F.C. Krebs, Stability/degradation of polymer solar cells. *Sol. Energy Mater. Sol. Cells* **92**, 686–714 (2008)
6. M. Jørgensen, K. Norrman, S.A. Gevorgyan, T. Tromholt, B. Andreasen, F.C. Krebs, Stability of polymer solar cells. *Adv. Mater.* **24**, 580 (2012)
7. T. Kuwabara, Y. Kawahara, T. Yamaguchi, K. Takahashi, Characterization of inverted type organic solar cells with a ZnO layer as the electron collection electrode by ac impedance spectroscopy. *ACS Appl. Mater.* **1**, 2107–2110 (2009)
8. J.L. Delgado, P.A. Bouit, S. Filippone, M.A. Herranz, N. Martin, Organic photovoltaics: a chemical approach. *Chem. Commun.* **46**, 4853–4865 (2010)
9. M.S. White, D.C. Olson, S.E. Shaheen, N. Kopidakis, D.S. Ginley, Inverted bulk-heterojunction organic photovoltaic device using a solution-derived ZnO underlayer. *Appl. Phys. Lett.* **89**, 1435171–1435173 (2006)
10. M.F. Malek, M.H. Mamat, M.Z. Sahdan, M.Z. Musa, Z. Khusaimi, M. Rusop, Influence of various sol concentrations on stress/strain and properties of ZnO thin films synthesised by sol-gel technique. *Thin Solid Films* **527**, 102–109 (2013)
11. M.F. Malek, M.Z. Sahdan, M.H. Mamat, M.Z. Musa, Z. Khusaimi, S.S. Husairi, N.D. Md Sin, M. Rusop, A novel fabrication of MEH-PPV/Al:ZnO nanorod arrays based ordered bulk heterojunction hybrid solar cells. *Appl. Surf. Sci.* **275**, 75–83 (2013)
12. A.K.K. Kyaw, X.W. Sun, C.Y. Jiang, G.Q. Lo, D.W. Zhao, D.L. Kwong, An inverted organic solar cell employing a sol-gel derived ZnO electron selective layer and thermal evaporated MoO₃ hole selective layer. *Appl. Phys. Lett.* **93**, 221107–221101–221107–221103 (2008)
13. Y.-J. Noh, S.-I. Na, S.-S. Kim, Inverted polymer solar cells including ZnO electron transport layer fabricated by facile spray pyrolysis. *Sol. Energy Mater. Sol. Cells* **117**, 139–144 (2013)
14. R. Lampande, G.W. Kim, D.C. Choe, J.H. Kong, J.H. Kwon, Solution processed n-type mixed metal oxide layer for electron extraction in inverted polymer solar cells. *Sol. Energy Mater. Sol. Cells* **125**, 276–282 (2014)
15. X. Yu, X. Yu, J. Zhang, G. Zhao, J. Ni, H. Cai, Y. Zhao, Efficiency boosting of inverted polymer solar cells with a polyvinylpyrrolidone-modified Al-doped ZnO electron transport layer. *Sol. Energy Mater. Sol. Cells* **128**, 307–312 (2014)
16. M. Thambidurai, J.Y. Kim, C.M. Kang, N. Muthukumarasamy, H.J. Song, J. Song, Y. Ko, D. Velauthapillai, C. Lee, Enhanced photovoltaic performance of inverted organic solar cells with In-doped ZnO as an electron extraction layer. *Renew. Energy* **66**, 433–442 (2014)
17. A. Baumann, T.J. Savenije, D.H.K. Murthy, M. Heeney, V. Dyakonov, C. Deibel, Influence of phase segregation on recombination dynamics in organic bulk heterojunction solar cells. *Adv. Funct. Mater.* **21**, 1687–1692 (2011)
18. F. Zhang, X. Xu, W. Tang, J. Zhang, Z. Zhuo, J. Wang, J. Wang, Z. Xu, Y. Wang, Recent development of the inverted configuration organic solar cells. *Sol. Energy Mater. Sol. Cells* **95**, 1785–1799 (2011)
19. M.Z. Sahdan, M.F. Malek, M.S. Alias, S.A. Kamaruddin, C.A. Norhidayah, N. Sarip, N. Nafarizal, M. Rusop, Fabrication of inverted bulk heterojunction organic solar cells based on conjugated P3HT:PCBM using various thicknesses of ZnO buffer layer. *Optik* **126**, 645–648 (2015)
20. M.J. Alam, D.C. Cameron, Preparation and properties of transparent conductive aluminum-doped zinc oxide thin films by sol-gel process. *J. Vac. Sci. Technol., A* **19**, 1642–1646 (2001)
21. B.D. Cullity, S.R. Stock, *Elements of X-ray Diffraction* (Addison-Wesley, Reading, 1978)
22. M.Z. Sahdan, M.H. Mamat, M. Salina, Z. Khusaimi, U.M. Noor, M. Rusop, Heat treatment effects on the surface morphology and optical properties of ZnO nanostructures. *Phys. Status Solidi C* **7**, 2286–2289 (2010)
23. E.F. Keskenler, M. Tomakin, S. Doğan, G. Turgut, S. Aydın, S. Duman, B. Gürbulak, Growth and characterization of Ag/n-ZnO/p-Si/Al heterojunction diode by sol-gel spin technique. *J. Alloys Compd.* **550**, 129–132 (2013)
24. B.D. Cullity, S.R. Stock, *Elements of X-ray Diffraction* (Prentice Hall, New Jersey, 2001)
25. T.P. Rao, M.C. Santhoshkumar, Effect of thickness on structural, optical and electrical properties of nanostructured ZnO thin films by spray pyrolysis. *Appl. Surf. Sci.* **255**, 4579–4584 (2009)
26. O. Lupan, T. Pauporté, L. Chow, B. Viana, F. Pellé, L.K. Ono, B. Roldan Cuenya, H. Heinrich, Effects of annealing on properties of ZnO thin films prepared by electrochemical deposition in chloride medium. *Appl. Surf. Sci.* **256**, 1895–1907 (2010)
27. Selected Powder Diffraction Data for Metals and Alloys, vol.1 (JCPDS, USA, 1978), p. 108
28. R. Ghosh, D. Basak, S. Fujihara, Effect of substrate-induced strain on the structural, electrical, and optical properties of polycrystalline ZnO thin films. *J. Appl. Phys.* **96**, 2689–2692 (2004)
29. V. Gupta, A. Mansingh, Influence of postdeposition annealing on the structural and optical properties of sputtered zinc oxide film. *J. Appl. Phys.* **80**, 1063–1073 (1996)
30. X.J. Ping, S.S. Bo, L. Lan, Z.X. Song, W.Y. Xin, C.X. Ming, Effects of annealing temperature on structural and optical properties of ZnO thin films. *Chin. Phys. Lett.* **27**, 047803 (2010)
31. Y.G. Wang, S.P. Lau, H.W. Lee, S.F. Yu, B.K. Tay, X.H. Zhang, K.Y. Tse, H.H. Hng, Comprehensive study of ZnO films prepared by filtered cathodic vacuum arc at room temperature. *J. Appl. Phys.* **94**, 1597–1604 (2003)
32. M.F. Malek, M.H. Mamat, M.Z. Musa, Z. Khusaimi, M.Z. Sahdan, A.B. Suriani, A. Ishak, I. Saurdi, S.A. Rahman, M. Rusop, Thermal annealing-induced formation of ZnO nanoparticles: minimum strain and stress ameliorate preferred c-axis orientation and crystal-growth properties. *J. Alloys Compd.* **610**, 575–588 (2014)
33. J. Rodríguez-Báez, A. Maldonado, G. Torres-Delgado, R. Castanedo-Pérez, M. de la, L. Olvera, Influence of the molar concentration and substrate temperature on fluorine-doped zinc oxide thin films chemically sprayed. *Mater. Lett.* **60**, 1594–1598 (2006)
34. M.F. Malek, M.H. Mamat, Z. Khusaimi, M.Z. Sahdan, M.Z. Musa, A.R. Zainun, A.B. Suriani, N.D. Md Sin, S.B. Abd Hamid, M. Rusop, Sonicated sol-gel preparation of nanoparticulate ZnO thin films with various deposition speeds: the highly preferred c-axis (0 0 2) orientation enhances the final properties. *J. Alloys Compd.* **582**, 12–21 (2014)
35. H. Hoppe, N.S. Sariciftci, Organic solar cells: an overview. *J. Mater. Res.* **19**, 1924–1945 (2004)
36. J. Rostalski, D. Meissner, Photocurrent spectroscopy for the investigation of charge carrier generation and transport mechanisms in organic p/n-junction solar cells. *Sol. Energy Mater. Sol. Cells* **63**, 37–47 (2000)
37. H.P. Kim, A.R.M. Yusoff, H.M. Kim, H.J. Lee, G.J. Seo, J. Jang, Inverted organic photovoltaic device with a new electron transport layer. *Nanoscale Res. Lett.* **9**, 150–150 (2014)

38. T.-H. Lai, S.-W. Tsang, J.R. Manders, S. Chen, F. So, Properties of interlayer for organic photovoltaics. *Mater. Today* **16**, 424–432 (2013)
39. H. Kim, K. Lee, Role of interpenetrating networks in the device performance of polymer-fullerene photovoltaic cells. *J. Korean Phys. Soc.* **42**, 183–186 (2003)
40. H. Sun, J. Weickert, H.C. Hesse, L. Schmidt-Mende, UV light protection through TiO₂ blocking layers for inverted organic solar cells. *Sol. Energy Mater. Sol. Cells* **95**, 3450–3454 (2011)